


RESEARCH ARTICLE

Semi-idealized simulations of wintertime flows and pollutant transport in an Alpine valley: Origins of local circulations (Part I)

Tiphaine Sabatier  | Alexandre Paci | Christine Lac | Guylaine Canut |
Yann Largeron | Valéry Masson

Centre National de Recherches
Météorologiques, Université de Toulouse,
Météo-France, CNRS, Toulouse, France

Correspondence

T. Sabatier, CNRM, Université de
Toulouse, Météo-France, CNRS, 42 av.
Gaspard Coriolis, 31057, Toulouse, France.
Email: tiphaine.sabatier@gmail.com

Funding information

The French Ministry of higher education
and research, CNRS (Centre National de la
Recherche Scientifique) and Météo-France

Abstract

Mountainous terrains are known for driving their own dynamics which respond to the local morphological arrangement of the area. Thermally driven flows in particular develop at slope and valley scales and ensure a certain degree of pollutant dispersion under quiescent wintertime synoptic conditions. The present study focuses on a section of the Arve River valley situated close to Mont Blanc which frequently suffers from severe pollution episodes under stable wintertime conditions whilst surrounding valleys appear to be less affected. The particular shape of this basin-like section and its location at the confluence of several tributary valleys raises the question of the extent to which local circulations participate in pollutant trapping over restricted sectors. A set of high-resolution numerical simulations are designed in order to improve our understanding of the local flow structure and their sensitivity to thermal stratification, radiative forcing and snow cover. The tributary valleys play a major role in both daytime and night-time dynamics by deflecting the entering daytime flux and constraining the night-time flow trajectories. In addition, the basin morphology greatly influences the circulations. During daytime a two-layer wind structure is developed and driven by spatial variations in sun exposure which is particularly heterogeneous under wintertime forcing. Early spring radiative forcing or the presence of snow allow both of them to develop more homogeneous circulations through the reduction of sun exposure variations, except when snow cover is restricted to shaded basin sidewalls. At night, a three-layer wind structure is developed. It favours air mass ventilation in the western linear branch of the basin whilst stagnation and recirculation prevail in the curved part of the valley which is also the most polluted. This study therefore highlights spatial variations in circulation patterns consistent with the accumulation of observed pollutants and their heterogeneous distribution.

KEYWORDS

air quality, Alpine valley, Passy-2015 field experiment, stable conditions, thermally driven circulation.

This is an open access article under the terms of the Creative Commons Attribution-NonCommercial License, which permits use, distribution and reproduction in any medium, provided the original work is properly cited and is not used for commercial purposes.

© 2019 The Authors. *Quarterly Journal of the Royal Meteorological Society* published by John Wiley & Sons Ltd on behalf of the Royal Meteorological Society.

1 | INTRODUCTION

Under quiescent synoptic conditions, mountainous terrains are associated with local dynamics which respond to topographic forcing (Whiteman, 2000; Lehner and Rotach, 2018; Serafin *et al.*, 2018). The first concepts concerning local thermally driven circulations were introduced in the middle of the 20th century by Wagner (1938) and Defant (1949). These studies described a wind reversal twice per day at the slope and valley scale in response to local density gradients under fair-weather conditions. Eighty years later, these concepts remain central but it is known now that the local dynamics strongly depend on orographic arrangement and the literature shows that this cannot be generalized from one valley to another (Rucker *et al.*, 2008; Duine *et al.*, 2017; Giovannini *et al.*, 2017). These local dynamics show a seasonal variability with solar forcing driving the relative period of daytime and night-time regimes (Bader and Whiteman, 1989; Whiteman, 2000; Zängl, 2004). Under wintertime conditions, the night-time regime assumes greater relative importance and participates in the formation of a strong temperature inversion drastically reducing the vertical mixing (Pernigotti *et al.*, 2007; Perrino *et al.*, 2014; Largeron and Staquet, 2016). Under these stable conditions, understanding of the local flows is crucial as they ensure a certain degree of ventilation and represent one of the only sources for pollutant redistribution over mountainous terrain (Steyn *et al.*, 2013).

At the slope scale, circulations emerge from differential warming/cooling between the near-surface air and the air at the same elevation in the valley centre. This mechanism drives the development of flow blowing up (anabatic) during the daytime period and down (katabatic) at night (Zardi and Whiteman, 2013). These systems depend on atmospheric thermal stability (Zhong and Whiteman, 2008; Retallack *et al.*, 2010; De Wekker and Kossmann, 2015) and surface properties through slope inclination, albedo or roughness length (Whiteman and Zhong, 2008; Nadeau *et al.*, 2013). At the valley scale, thermally driven flows respond to horizontal pressure gradients which develop in response to the evolution of along-valley morphological features (Rampanelli *et al.*, 2004). These gradients drive up-valley winds (UVWs) during the daytime period which reverse to down-valley winds (DVWs) at night. These systems are locally adapted depending on the topographic arrangement and the land cover features. For instance, numerous idealized numerical studies have shown that the UVW depends on valley width and bottom slope inclination governing the air volume at work and thus the difference of temperature driving the system (Rampanelli *et al.*, 2004; Serafin and Zardi, 2010;

Wagner *et al.*, 2015a; 2015b). In addition, along-valley variations such as local constrictions induce a local flow acceleration to ensure mass conservation (Zängl, 2004), while orographic depression may generate pressure anomalies in turn modifying the flow intensity (Rucker *et al.*, 2008; Giovannini *et al.*, 2017). The valley orientation also represents a key parameter since it governs the short-wave radiation distribution and thus the pressure field. Spatial variation in sun exposure may induce a secondary breeze perpendicular to the valley axis and orientated towards the sunlit sidewall (Bader and Whiteman, 1989; Gohm *et al.*, 2009; Harnisch *et al.*, 2009). Anomalies in the flow structure may also be generated by local topographic curvature (Weigel and Rotach, 2004; Weigel *et al.*, 2006) or tributary valleys which may drive their own thermally driven wind systems. For instance, a tributary valley can deviate a fraction of the UVW during the day (Zängl, 2004) or nourish the DVW developed within the main valley at night (Porch *et al.*, 1989; O'Steen, 2000). Under stable conditions, this convergence may induce a multi-layered vertical structure due to the arrival of air mass with varied densities (Alexandrova *et al.*, 2003; Pardyjak *et al.*, 2009; Largeron, 2010). At a finer scale, the land cover also influences local flows through the micro-system generated by the mosaic of ground texture (Whiteman, 2000). For instance the presence of a town, lake or sea can generate secondary thermally driven breezes which may reinforce or inhibit the orographic wind system (Crosman and Horel, 2010; Rendón *et al.*, 2014; Leo *et al.*, 2015; Giovannini *et al.*, 2017). In addition, the presence of snow is recognized as a key parameter, since it increases the surface albedo and decreases the heat transfer from the ground (Billings *et al.*, 2006; Silcox *et al.*, 2012). This reduction in energy input tends to reinforce the temperature inversion strength and favours the down-valley and down-slope regimes (Zardi and Whiteman, 2013). Finally, the complexity of the local flow analysis lies in the multiple components which compose the system and are driven by various local and non-local parameters.

The present study focuses on local circulations which develop within a section of the Arve River valley situated in the French Alps in the vicinity of the Mont Blanc. This valley includes a semi-enclosed basin which is characterized by a high degree of complexity with a particular billhook shape located at the confluence of several tributary valleys. A better understanding of the local dynamics is necessary since the area is one of the worst places in France in terms of air quality with severe PM10 pollution episodes frequently occurring under wintertime anticyclonic conditions. The influence of thermal stratification on pollution has been studied by Chemel *et al.* (2016) through the comparison of hourly and daily PM10 concentrations

with a vertically integrated measure of atmospheric stability (heat deficit defined by Whiteman *et al.* (1999)). The authors highlighted a good correlation at the daily scale with $R^2 = 0.69$. Hourly analysis is less clear ($R^2 = 0.31$), suggesting that the processes at play cannot be understood only by considering the thermal stratification of the basin. Circulations and transport processes developed from meso- γ (mountain-valley) to micro- α (slope) scales, according to the terminology of Lehner and Rotach (2018), must therefore be considered for this area halfway between a valley and a basin, the latter being known to inhibit the along-valley circulation (Clements *et al.*, 2003; Whiteman *et al.*, 2004; Arduini *et al.*, 2017). A first analysis based on scanning Doppler lidar measurements acquired during the Passy-2015 field experiment (Paci *et al.*, 2016) has allowed the characterization of an along-valley wind system and has raised several questions about the complex flow layout (Sabatier *et al.*, 2018). At this point, numerical models represent a complementary tool for observations for the determination of mechanisms governing the circulation structure in this highly complex terrain. The present study is therefore based on a set of high-resolution numerical simulations run in a semi-idealized framework (realistic orography, simplified initialization, no large-scale forcing) so as to focus on local thermally driven circulations. This configuration represents a complementary approach to the usual real-case simulations where all the complex characteristics are embedded and difficult to separate from each other. A reference simulation is designed in order to reproduce simplified conditions encountered during a wintertime local pollution episode and to improve our understanding of the observed wind structure. In addition, various experiments are conducted to determine to what extent the circulations are modified by weaker initial stratification, early spring radiative forcing or snow-covered situations. Using the model as a laboratory is a powerful tool for improving our understanding of the processes. The consequences of the dynamics on pollutant transport will be further discussed in a companion paper (Sabatier *et al.*, 2020, referred to as Part II in the following), which constitutes the ultimate goal of the study.

The paper is organized as follows: the investigated area, the observations and the simulations are presented in Section 2. Section 3 provides an overview of the observed wind structures on which is based the numerical experiment strategy. A brief comparison of the observed and simulated wind patterns is proposed in Section 4, while the numerical experiment analysis is carried out in Section 5. Conclusions and questions raised in relation to pollutant transport are drawn in Section 6.

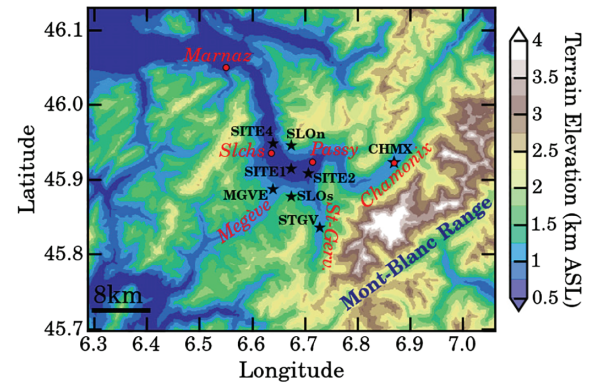


FIGURE 1 Domain of interest with the main cities and valleys indicated in red, the air quality stations by red dots and the measurement and vertical profile sites by black stars

2 | OBSERVATIONS AND MODEL SET-UP

2.1 | Site of interest

The present study focuses on a restricted section of the Arve River valley located in the French Alps in the vicinity of Mont Blanc. The region of interest can be decomposed into several sectors with the Passy basin and its billhook shape located in the centre of Figure 1. This semi-closed basin has an average bottom elevation of 560 m above sea level (a.s.l.), a maximum width of 2 km at the ground level and an average depth of 1,000 m. It can be decomposed into two parts with an eastern curved section oriented east–west including the city of Passy and a western straight section of about 16 km long oriented south–north and including the city of Sallanches. The basin is connected with a wider downstream section to the northwest starting with the city of Marnaz, the upstream Chamonix valley to the east, the Megève and Saint-Gervais valleys to the south. In the following Megève, Saint-Gervais and Chamonix valleys will be referred to as tributary valleys.

In winter, this area frequently experiences pollution episodes which do affect the various valleys with differing severity. For instance, during the winter of 2014–2015, the number of days exceeding the PM₁₀ threshold for air quality monitoring (daily $[PM_{10}] > 50 \mu\text{g}\cdot\text{m}^{-3}$) were: 44 days for Passy, 20 for Sallanches, 10 for Chamonix and 3 for Marnaz, according to the local air quality agency Atmo-Auvergne Rhones-Alpes (Atmo-AURA, 2015). Similar dynamics were also observed over the last 10 years, thereby underlining a recurring air quality issue. The high level of pollutants measured within the basin and the significant basin-scale heterogeneities in pollutant

concentration raise the question of the influence of local dynamics on pollution accumulation. This question was the motive for the Passy-2015 field experiment which took place during the winter 2014–2015 (Paci *et al.*, 2016). The present study is in line with this objective and focuses on local circulations and basin-scale heterogeneity which may determine the pollutant trapping over restricted sectors. More precisely, this paper focuses on conditions encountered during two important anticyclonic episodes documented during the Passy-2015 field experiment:

- A severe wintertime pollution episode from 6 to 14 February 2015 (IOP1) was the strongest pollution episode observed during the Passy-2015 field experiment. This situation combined wintertime radiative forcing, snow cover, clear-sky conditions and persistent temperature inversion. During this period, daily average PM10 concentrations larger than $80 \mu\text{g}\cdot\text{m}^{-3}$ and nocturnal hourly PM10 concentrations of more than $160 \mu\text{g}\cdot\text{m}^{-3}$ were measured within the basin, while concentrations recorded in the Chamonix valley were lower than $40 \mu\text{g}\cdot\text{m}^{-3}$ as a daily average (not shown).
- A lighter pollution episode occurring under clear-sky conditions between 7 and 13 March 2015. This early spring episode was associated with overall lower PM10 concentrations which never exceeded $55 \mu\text{g}\cdot\text{m}^{-3}$ as a daily average within the basin.

The difference in pollution severity between these two episodes, occurring only one month apart, raises the question of the relative influence of emission features and wind dynamics evolution. The present study therefore aims to understand the local circulations developed under these conditions by comparing a typical day for each episode (a) firstly from observations acquired during the field experiment, and (b) in a more extensive way from a set of numerical experiments.

2.2 | Observations

Data from the Passy-2015 field experiment are used to analyse the flow structure within the basin during both episodes, to highlight the main differences and to initialize numerical simulations. A summary of the sensors used in this paper is given in Table 1 while the complete list can be found in Paci *et al.* (2016).

The flow structure in the basin centre (SITE1) is characterized by a combination of four sonic anemometers deployed on a 10 m mast and a profiler Doppler wind lidar (WLS8-5) which provides measurements from 40 m up to 500 m above ground level (a.g.l.). In addition, a scanning Doppler wind lidar deployed at SITE2 provides spatialized

measurements of line-of-sight velocity (V_{los}) with an atmospheric volume documented every hour. This database has been investigated in depth by Sabatier *et al.* (2018) who provided an observation-based analysis of the wind structure during the persistent stage of the IOP1 of the Passy-2015 field experiment. Potential temperature and humidity profiles were measured at SITE1 by radiosoundings launched every 3 hr with a 10 m interpolated resolution during IOPs or retrieved from microwave radiometer (MWR) measurements available every 6 min with a 50 m vertical resolution.

2.3 | Numerical simulations

High-resolution mesoscale simulations (based on the Cuxart (2015) terminology) were performed with the non-hydrostatic anelastic atmospheric research model Meso-NH (Lac *et al.*, 2018). This model has already shown its performance in reproducing the dynamics over complex terrain from mesoscale simulations (Stein, 2004; Largeron, 2010; Jiménez *et al.*, 2019) to large-eddy simulations (LESs) (Vionnet *et al.*, 2014; Blein, 2016; Brun *et al.*, 2017; Vionnet *et al.*, 2017). In addition, the IOP1 of the Passy-2015 field experiment has been simulated with Meso-NH in an on-going study which shows satisfying results in the reproduction of the temporal evolution of the temperature inversion within the basin (Y. Largeron, personal communication, 2019). Most of these studies were based on a real-case configuration with initial and forcing fields provided by analyses or forecasts from a numerical weather prediction (NWP) model with a down-scaling approach by grid-nesting. The objective here is to characterize the relative importance of processes on wind dynamics. We favour therefore the use of a semi-idealized framework based on the set-up of the on-going Largeron's study but in simplified initial and coupling conditions in order to avoid the complexity of the interactions between large-scale and local forcing and to use the model as a laboratory through which to perform sensitivity analyses.

2.3.1 | Numerical set-up

In the present study, Meso-NH uses a *forward-in-time* temporal scheme, the fourth-order centered scheme for momentum advection and the Piecewise Parabolic Method (PPM; Colella and Woodward, 1984) for meteorological and scalar variable advection. The model relies on a 1D radiative scheme based on Fouquart and Bonnel (1980) equations for short-wave radiations and on the Rapid Radiative Transfer Model (RRTM; Mlawer *et al.*, 1997) for long-wave radiation. Shading effects

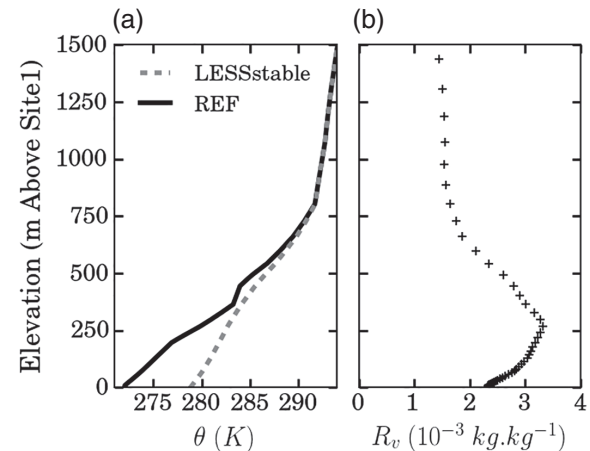
TABLE 1 Summary of the sensors deployed during the Passy-2015 field experiment used in this paper, along with the parameters measured and their spatial and temporal resolutions

Site	Location Coord. (N, E)	Elevation (m a.s.l.)	Sensor	Variables	Spatial/temporal resolution
1	45.914, 6.674	560	Sonic anemometer HS50 (Gill)	u, v, w	Local/1 min
			Profiler Doppler wind lidar WLS8-5 (Leosphere)	u, v	$\Delta_z=20$ m/3 s
			Radiosonde RS92-SGP (Vaisala)	Temp., RH	$\Delta_z=10$ m/3 hr
			Microwave radiometer HATPRO (RPG)	Temp.	$\Delta_z=50:200$ m/6 min
2	45.908, 6.707	602	Scanning Doppler wind lidar WLS200S (Leosphere)	\mathbf{V}_{los}	$\Delta_{los}=100$ m/1 hr

are considered through the modification of the direct downward short-wave (SW) fluxes according to the slope and orientation of the orography with respect to the azimuthal and zenithal solar angles. The 3D turbulence scheme described by Cuxart *et al.* (2000) is used with a prognostic equation for turbulent kinetic energy (TKE; 1.5 closure) and the diagnostic mixing length of Deardorff (1974) given by the volume-average grid size reduced by stratification. The ICE3 one-moment mixed microphysical scheme (Pinty and Jabouille, 1998) is activated but no fog formed in the simulations. The model is coupled with the externalized platform SURFEX (Surface Externalisée; Masson *et al.*, 2013) to account for interactions between surface and atmosphere.

The simulation domain presented in Figure 1 covers a surface of 60×48 km² with a horizontal resolution of 100 m. This domain includes the Mont Blanc range and the tributary valleys surrounding the basin. In the vertical, 72 levels are defined using a terrain-following coordinate system (Gal-Chen and Somerville, 1975), with a 2 m resolution at the first level and a stretching of 10% in the first 1,000 m and 20% aloft. The fine resolution of the first levels is chosen according to Blein (2016) who recommended 2 m as the resolution required to ensure the realism of slope wind systems. An absorbing layer is activated at the domain upper boundary located at 20 km a.s.l. in order to prevent the reflection of gravity waves. Lateral boundary conditions are open, letting the short-scale waves out of the domain with minimal reflection at the boundaries. To ensure the realism of the flows developed in the vicinity of the basin, the domain is extended significantly beyond the domain of interest.

The orography is issued from the 90 m resolution Shuttle Radar Topography Mission (SRTM) database. A local smoothing is applied to the slopes with an inclination above 45 in order to ensure the convergence of the pressure solver due to the anelastic approximation. This correction affects a restricted area of the domain (around 6%) concerning mainly the steep cliffs of the mountain ranges bordering the basin. The Ecoclimap-II database is used to specify land cover with a kilometre resolution (Faroux

**FIGURE 2** Initial profiles of (a) potential temperature and (b) water vapour mixing ratio specified at SITE1. The black profiles measured by radiosounding during the IOP1 episode are used for the initialization of simulations REF, MARCH, SNOW and SNOWsouth, while the LESSstable simulation is initialized with the grey potential temperature profile measured by MWR during the March episode

et al., 2013). The domain is mainly composed of natural cover (97%), the remaining percentages being composed of urban patches within valleys.

2.3.2 | Reference simulation

The reference simulation (REF) starts at 0900 UTC on 11 February 2015 and is integrated for 39 hr yielding the full diurnal cycle of 12 February 2015. The atmosphere initialization requires profiles of potential temperature, humidity and horizontal wind which are specified at the basin centre (SITE1) and then interpolated vertically and horizontally over the entire grid. An initial zero-wind profile is forced to let the thermally driven dynamics build up as proposed by Colette *et al.* (2003), Lehner and Gohm (2010) and Wagner *et al.* (2015a). Potential temperature and humidity profiles are specified from radiosounding profiles measured during IOP1 of the Passy-2015 field experiment (Figure 2). The initial fields are used for the

prognostic variables to be relaxed in the top absorbing layer to prevent the reflection of orographic waves, and at the lateral boundary conditions for normal wind through the Carpenter treatment (equation 6 of Lac *et al.*, 2018). Apart from the boundary conditions, the large-scale forcing is equal to zero in order to dispense with large-scale perturbations (Zängl, 2004). This means that there is no large-scale tendency applied to the prognostic variables across the whole domain. The initial sea level pressure is set to 1030.35 hPa.

The surface is composed of three ground layers, each one requiring the initialization of temperature, water and ice contents. In the absence of measurement, the temperature of the surface layer is initialized so as to be in balance with the first atmospheric level at SITE1. An increment of 1 K is added to the two lower layers. These surface temperatures are then vertically interpolated with elevation using $-6.5 \text{ K}\cdot\text{km}^{-1}$ as a gradient, this method delivering better results than a homogeneous surface temperature field in mountainous terrain as shown by Chow *et al.* (2006). The water/ice ratio is set to 0.8/0.2 for the surface layer and 1.0/0.0 for the two lower layers. No snow cover is considered in the reference simulation, except for a few patches of permanent snow at the top of Mont Blanc. The model time step is set to 1 s while 3D fields are saved every 30 min. In addition, vertical profiles at selected locations are saved every 3 min in order to get better time resolution of the dynamics. The profile locations are shown by black stars in Figure 1.

2.3.3 | Numerical experiments

In the following, the reference (REF) simulation will be considered as representative of simplified conditions encountered during the stagnation stage of IOP1 of the Passy-2015 field experiment. This simulation will be used (a) to improve our understanding of the observed wind structures, and (b) to serve as a reference for comparison with numerical experiments designed to determine the influence of several processes on wind dynamics. The set of simulations aims to quantify the relative influence of the initial thermal stability profile (LESSstable), radiative forcing (MARCH) and snow cover (SNOW and SNOWsouth) :

- In the LESSstable simulation, a less stratified initial atmosphere is prescribed in order to determine the impact of the initial stratification on wind dynamics. The potential temperature is initialized from a profile measured by MWR during the March case (Figure 2) leading to an initial Brunt–Väisälä frequency in the first 500 m a.g.l. of 0.023 s^{-1} instead of 0.032 s^{-1} in REF.

- In the MARCH simulation, the initialization state is the same as in REF, but the radiative forcing of 9 March is used instead of that of 12 February in order to quantify the seasonal evolution between wintertime and early spring conditions. This difference represents an increase of 46% in the total energy received at SITE1 over a complete diurnal cycle (Figure 1 shows the SITE1 location).
- The influence of snow cover is investigated by the SNOW simulation for which a homogeneous snow cover of 30 cm is initialized across the entire domain.
- The importance of the snow cover state is evaluated by considering a snow cover restricted to the southern shaded slopes of the basin in the SNOWsouth simulation.

In the absence of a high-resolution snow cover field, the last two simulations allow the investigation of the influence of snow by considering simplified conditions inspired from those encountered during the IOP1 with an initial homogeneous cover (SNOW) that progressively melts along the sunlit sidewall (SNOWsouth) thereby creating a north–south heterogeneity. The determination of the impact of snow on the local dynamics is a matter of general interest since the previously described snow cover evolution may be relevant for other wintertime pollution episodes in the basin and more generally in every valley sharing a west–east orientation.

3 | PRELIMINARY RESULTS FROM OBSERVATIONS

This first section of results provides an overview of the main differences between the along-valley circulation observed during a typical day of the IOP1 and the March episodes using the Passy-2015 field experiment database. The strategy for the numerical experiments presented in the following sections is based on these observations. These observations, along with those presented in Sabatier *et al.* (2018), are also important for supporting the relevance of the numerical simulations for studying the situations behind these two pollution episodes.

3.1 | Daytime dynamics

Wind measurements from sonic anemometer and profiler Doppler wind lidar are used to investigate the vertical structure of the flows in the basin centre (SITE1) between 2.5 and 500 m a.g.l.. Wind roses at 10, 40 and 100 m a.g.l. are represented in Figure 3 for a day of the (a, b, c) IOP1

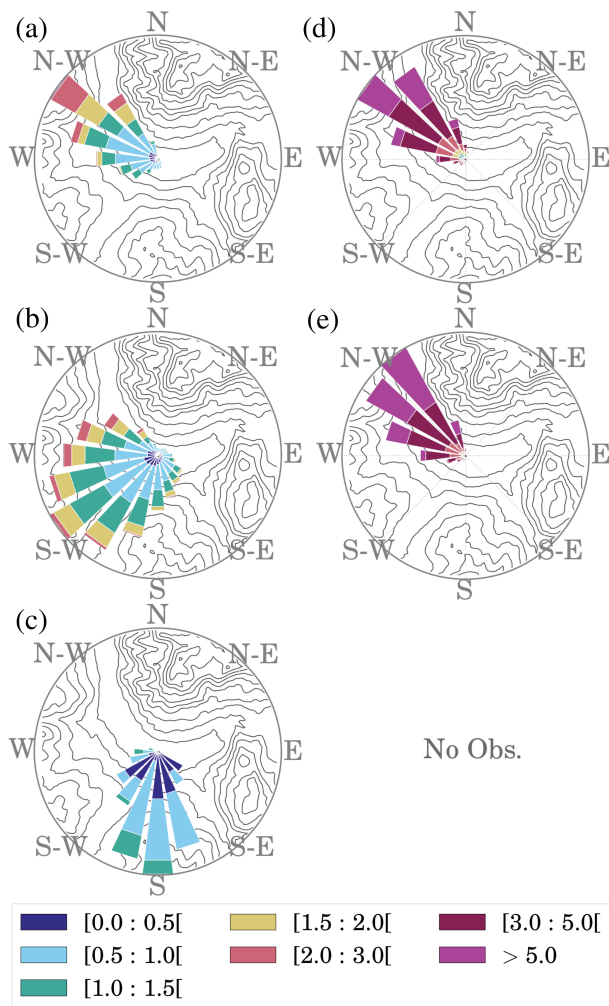


FIGURE 3 Daytime-averaged wind roses determined over the 1000–1700 UTC period at (a,d) 100 m, (b,e) 40 m and (c) 10 m a.g.l. at SITE1 during a typical day of the (a, b, c) IOP1 and (d, e) March episodes, both documented during the Passy-2015 field experiment. Wind intensity ranges are given in $\text{m}\cdot\text{s}^{-1}$. Topographic contours are shown in grey

and (d, e) a day in the March episode. The wind patterns observed during these selected days are representative of their associated episodes. The wind roses are determined across the 1000–1700 UTC interval corresponding to the period of UVW establishment during the IOP1 as reported by Sabatier *et al.* (2018).

At 100 m a.g.l., the wind in the basin centre is oriented up-valley in both situations, as expected from theoretical concepts (Defant, 1949; Zardi and Whiteman, 2013). In February, another component is observed near the surface with a southerly wind measured at 10 m a.g.l. (Figure 3c) leading to a two-layer wind structure. At 40 m a.g.l. (Figure 3b), a transient flow is observed between the lower southerly wind layer and the upper regular UVW aligned with the local basin axis aloft (Figure 3a). In March, there is no measurement available within the

first 10 m above ground level but the 40 m a.g.l. wind rose (Figure 3e) clearly shows a component aligned with the basin axis, signifying that the UVW has reached the lower altitude and has become the dominant component at this elevation. This evolution may be associated with at least a reduction or even an extinction of the lower southerly wind component. A noticeable reinforcement of the UVW intensity is also observed during this episode with wind intensity in the range $3\text{--}6\text{ m}\cdot\text{s}^{-1}$ instead of $1\text{--}3\text{ m}\cdot\text{s}^{-1}$ during IOP1. In addition, measurements from the profiler Doppler wind lidar show that the UVW layer becomes more developed in the vertical, leading to an average thickness of 450 m during the March episode and 200 m during the IOP1 episode (not shown). This more intense and more developed UVW still has a thermal origin as the transition hours between up- and down-valley wind systems remain constant during the episode which is evidence of thermally driven circulation (Whiteman and Doran, 1993). Additionally, it was observed during every day of the March episode regardless of the large-scale conditions (not shown).

3.2 | Night-time dynamics

Figure 4 represents south–north cross-sections of line-of-sight fields (V_{los}) established from horizontal scans at several elevations measured by the scanning Doppler lidar. Due to the lidar location at SITE2, these fields can be considered as representative of the along-valley wind system. (Sabatier *et al.*, 2018 give more details about the scanning strategy.) These fields are averaged over the 2100–0800 UTC period leading to the average night-time along-valley flow during a typical night of the IOP1 and of the March episode (cf. Figures 4a and b).

During the IOP1, a complex flow layout is observed with:

- a quiescent atmosphere in the lowest layer between 600 and 700 m a.s.l. associated with average intensities lower than $0.5\text{ m}\cdot\text{s}^{-1}$. These weak intensities result from a strong thermal stability which prevents the DVW from reaching the low levels within the basin, leaving mainly weak wind oscillations in the near-surface basin atmosphere.
- a DVW aloft with a jet shape and a maximum velocity of $1\text{ m}\cdot\text{s}^{-1}$ observed at 740 m a.s.l. This jet shows a particular trajectory since it remains along the northern basin sidewall while an opposite up-valley flow is observed in the southern sector.

Instead of $0.5\text{ m}\cdot\text{s}^{-1}$ reached during the IOP1, during the March episode the jet flows at lower altitude

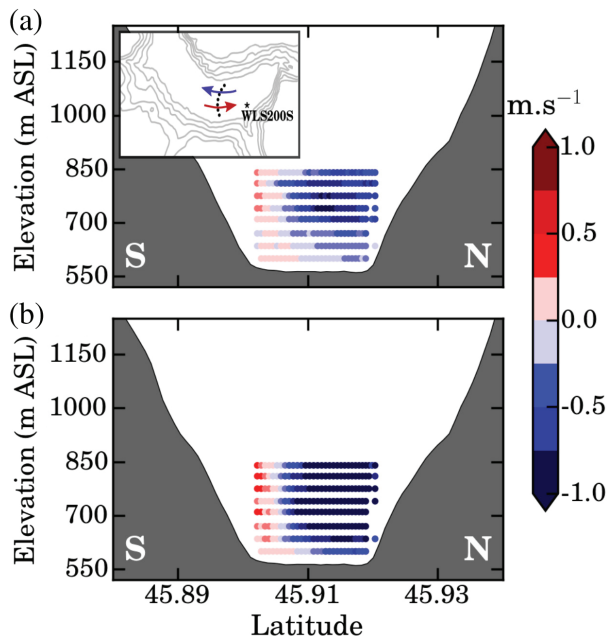


FIGURE 4 Night-time-averaged south–north cross-sections of line-of-sight velocity (V_{los}) extracted from horizontal scans at several elevations from the scanning Doppler lidar (WLS200S). The fields are determined over the 2100–0800 UTC period for a typical night in (a) the stagnation stage of IOP1, and (b) the March episode, both documented during the Passy-2015 field experiment. Down-valley flows have negative values (blue) while up-valley flows have positive values (red)

(Figure 4b) become more intense, with a mean jet averaged over 45.91–45.92N reaching $1 \text{ m}\cdot\text{s}^{-1}$. The jet lowering may be explained by a reduced night-time thermal stratification allowing the jet to penetrate deeper within the lower basin atmosphere. Quantitatively, the vertical gradient of potential temperature ($d\theta/dz$) determined at 2100 UTC within the first 50 m above the ground level at SITE1 is equal to $8.4 \text{ K}\cdot(100 \text{ m})^{-1}$ in February instead of $4.5 \text{ K}\cdot(100 \text{ m})^{-1}$ in March (using radiosounding and MWR measured profiles respectively). This evolution tends to reduce the thickness of the near-surface quiescent layer thereby reducing the night-time atmosphere stagnation.

4 | EVALUATION OF THE FLOWS DEVELOPED IN THE REF SIMULATION

The numerical framework being semi-idealized, we intend the simulations to reproduce the main observed circulation patterns but not necessarily the exact details and intensities. This is verified in the current section through a brief comparison of the flows observed during the IOP1 and simulated in the REF simulation.

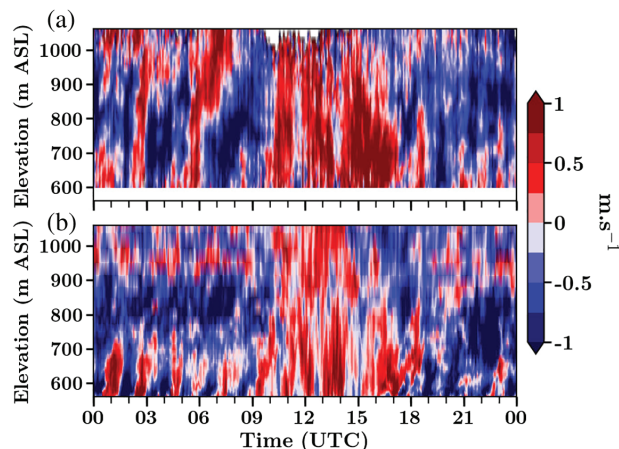


FIGURE 5 Time–elevation diagram of zonal wind component during a typical day of the IOP1 extracted at SITE1 (Figure 1) from (a) measurements of a profiler Doppler wind lidar (WLS8-5) deployed during the Passy-2015 field experiment, and (b) the REF simulation. Negative values (blue) are associated with down-valley flows while positive values (red) are associated with up-valley flows

Figure 5 represents time–elevation diagrams of zonal wind component from measurements (profiler Doppler wind lidar WLS8-5) during a typical day of the IOP1 and from the REF simulation (Figures 5a, 5b respectively). Both profiles are extracted at SITE1 whose location is indicated in Figure 1. Figure 5 highlights the model ability to reproduce the along-valley wind reversal despite some discrepancies in wind intensities. Indeed, the observed and simulated transition from DVW to UVW occurs around 1000 UTC while the UVW reverses to DVW around 1700 UTC. Figure 5 also underlines a correct reproduction of the nocturnal two-layer wind structure reported from observations with a lower layer mainly driven by wind direction oscillations and an upper layer in which the DVW prevails. On average over the night-time period (2100–0800 UTC), the simulated DVW vertical structure corresponds with the observed one, as can be seen by comparing Figures 4a and 6a. The latter represents a time-averaged (2100–0800 UTC) vertical cross-section of the simulated along-valley wind structure in the curved sector of the basin. A deeper analysis of the DVW trajectory will be addressed in section 5.2.

The model is also able to reproduce the observed daytime near-surface southerly wind component introduced in Figure 3c. This is illustrated in Figure 7a, which represents the 10 m a.g.l. wind rose determined across the 1000–1700 UTC period in the REF simulation. The origin of this fine-scale component will be further investigated in section 5.1.3 as it plays an important role in pollutant dispersion (Part II).

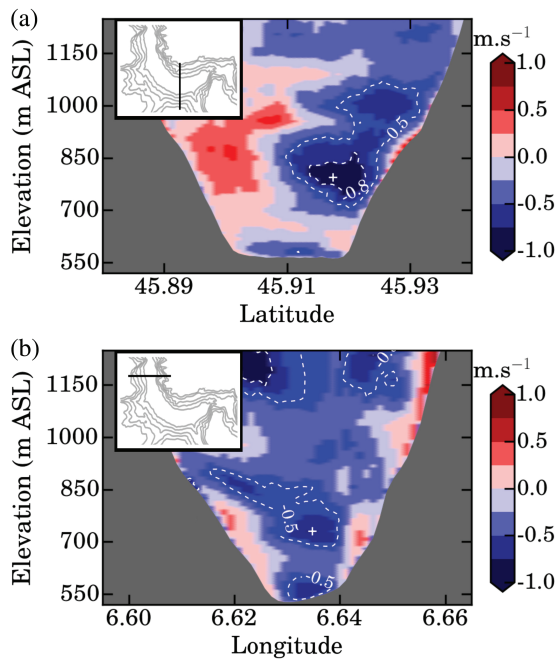


FIGURE 6 Night-time-averaged (2100–0800 UTC) vertical cross-sections of the along-valley wind structure determined over (a) a south–north cross-section in the central curved sector and (b) a west–east cross-section in the western branch of the basin in the REF simulation. The cross-section positions are indicated in the insets along with local orography. Red (blue) represents wind which goes up (down) along the local basin axis. The down-valley jet maxima are indicated by white crosses whilst iso-intensity is represented by white dashed contours.

Despite a simplified model initialization, the main simulated wind patterns are in agreement with the observed ones. Numerical simulations can therefore be used to improve our understanding of the processes at work.

5 | RESULT FROM NUMERICAL SIMULATIONS

In this section, simulated flows and processes are analysed first at the slope scale and then at the valley scale.

5.1 | Slope scale

5.1.1 | Temporal Evolution

Figure 8 represents the time evolution over the second day of all the simulations of the 7 m along-slope wind component determined along the southern and northern basin sidewalls (at SLOs and SLOn located respectively at the south and north of SITE1, as shown by Figure 1). The 7 m

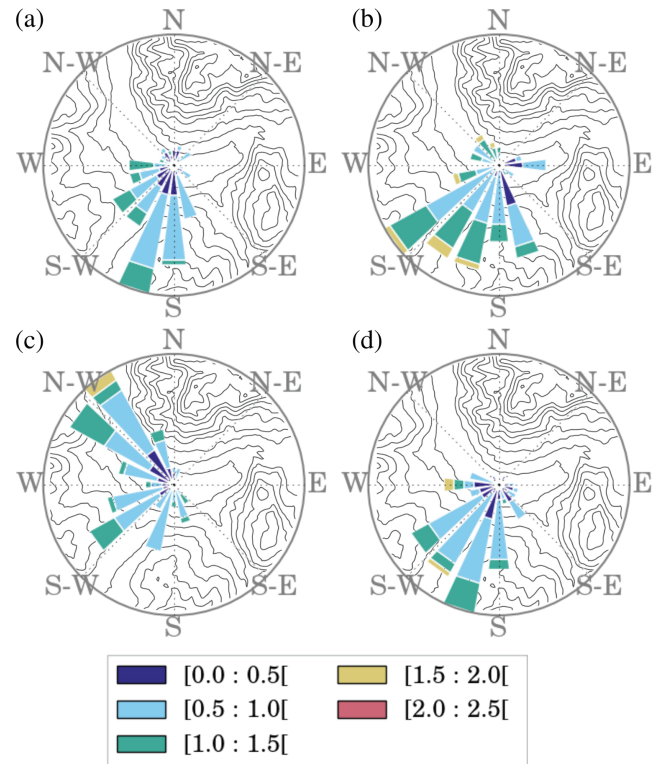


FIGURE 7 Daytime-averaged (1000–1700 UTC) wind roses extracted at 10 m a.g.l. in the basin centre (SITE1) for simulations (a) REF, (b) MARCH, (c) SNOW and (d) SNOWsouth. Wind intensity ranges are provided in m.s^{-1} . Topographic contours are drawn in grey

elevation is chosen because it corresponds to the average elevation of the anabatic wind maximum (Figure 9).

During daytime, an anabatic regime is developed over the northern slope in every simulation and lasts between 0800 and 1600 UTC in REF (Figure 8b). In MARCH, the anabatic regime lasts an hour and a half longer (0720–1700 UTC) than in REF while in SNOW the anabatic wind intensity is reduced. Along the southern slope (Figure 8a), a katabatic regime persists over the entire day for all simulations except MARCH, in which a substantial anabatic regime develops between 0900 and 1600 UTC. This highlights a first important characteristic of the winter season during which the southern slope mainly remains in the shade leading to a daily total cumulative energy insufficient for the reversal of the slope circulation (5.7×10^6 J received at the PSLOs site instead of 27.7×10^6 J at the PSLOn site in the REF simulation). At night, the main difference regarding the katabatic regime occurs in the early evening with a slight intensification in MARCH. Apart from that, similar behaviour is observed in all the simulations. For this reason, the remainder of this section will focus on the anabatic regime.

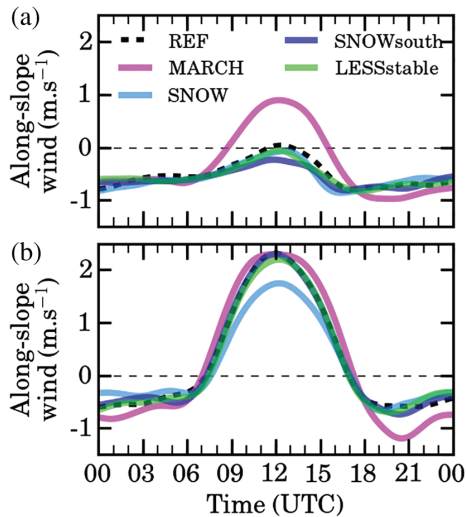


FIGURE 8 Temporal evolution of the 7 m a.g.l. along-slope wind component developed along the (a) southern (SLOs) and (b) northern (SLOn) basin sidewalls for all the simulations. SLOn and SLOs locations are indicated by black stars in Figure 1. Anabatic winds are counted as positive while katabatic winds are counted as negative

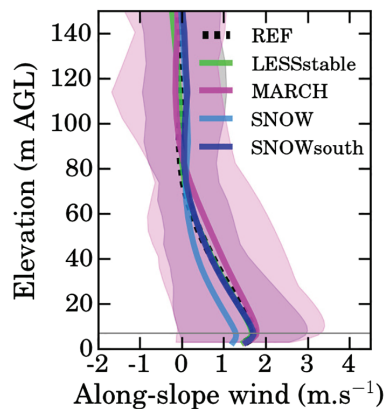


FIGURE 9 Daytime-averaged vertical structure of the anabatic winds developed along the northern sidewall (SLOn) for every simulation. The grey and pink envelopes gather all anabatic profiles for simulations REF and MARCH respectively

5.1.2 | Vertical Structure

Figure 9 represents the time-averaged vertical structure of anabatic winds developed along the northern basin sidewall (SLOn; Figure 1). The average is made for each simulation over the period for which anabatics are actually present. In addition, the profile envelopes are added for simulations REF and MARCH.

In the REF simulation, the anabatic winds developed vertically over 80 m with a maximum intensity around 7 m a.g.l.. The field experiment lacks data on the slope for comparison, but this simulated structure is coherent

with those reported in the literature (Zardi and Whiteman, 2013). In the MARCH simulation the anabatic winds intensity slightly while the opposite occurs in the SNOW simulation. There are no noticeable changes in the simulations SNOWsouth (in which there is no snow on the northern basin sidewall as in REF) and LESSstable.

5.1.3 | Spatial organization

Figure 10 represents the time-averaged horizontal wind vector determined over the 1000–1700 UTC period at 7 m a.g.l. with a southerly (westerly) wind pointing towards the top (right). This figure illustrates the anabatic principal location in each simulation.

In the REF simulation (Figure 10a), anabatic winds mainly developed along the south- and west-facing slopes. Figure 10a also underlines differences in the wind orientation developed at the basin bottom under the influence of the along-slope circulation. In the eastern curved part of the basin, the wind is mainly aligned with the anabatic winds running along the south-facing slopes, so it is orthogonal to the valley axis, whereas in the western linear section a more regular up-valley wind aligned with the valley axis is simulated. Note that a well-aligned flow is also developed within the Megève valley, but it rather corresponds to the along-valley wind system. In the MARCH simulation, the early spring radiative forcing allows the anabatic winds to develop over the entire basin slopes, even along the north-facing ones (Figure 10b). However intensity heterogeneities still persist in response to differences in sun exposure. The impact of snow cover (difference between REF and SNOW simulations; Figure 10c) is an overall weakening of along-slope circulation which is in line with the literature (Whiteman, 2000; Lehner and Gohm, 2010). Unsurprisingly, when snow cover is restricted to the north-facing slopes (difference between REF and SNOWsouth simulations; Figure 10d) there is no noticeable change in the along-slope circulation on the opposite slopes relative to the reference simulation.

The differences in the along-slope circulation can be used to analyse the cause of the near-surface southerly wind layer observed in the basin centre during the IOP1 of the Passy-2015 field experiment (Figure 3c). This component is reproduced in the REF simulation as shown in Figure 7a which represents the time-averaged (1000–1700 UTC) wind rose at 10 m a.g.l. at SITE1. This near-surface component can be related to the absence of anabatic wind along the southern slopes and presence along the northern slopes causing a mass flux divergence within the basin. This near-surface divergence drives the near-surface southerly wind. Its sensitivity to radiative forcing or snow cover is analysed from the time-averaged

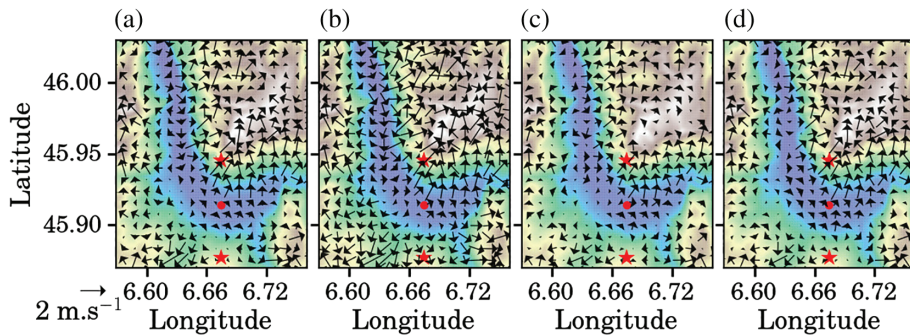


FIGURE 10 Daytime-averaged (1000–1700 UTC) horizontal wind vector at 7 m a.g.l. for the simulations (a) REF, (b) MARCH, (c) SNOW and (d) SNOWsouth. The red dot indicates the location of SITE1 while PSLOn and PSLOs sites are represented by red stars

(1000–1700 UTC) wind roses determined at 10 m a.g.l. in simulations MARCH, SNOW and SNOWsouth, Figures 7b, c and d respectively. In the MARCH simulation, even if anabatic winds develop along the southern slopes, a south–north gradient remains in the intensity and allows the near-surface southerly wind to persist. However the flow orientation slightly evolves from south in REF to a southwest direction in MARCH (Figure 7b). This may be related to the impact of the intensified UVW aloft which takes progressively greater relative importance. In the SNOW simulation, the near-surface southerly wind almost disappears in response to the weakening of the south–north intensity gradient. The 10 m wind at SITE1 thus becomes more aligned with the local basin axis (Figure 7c). It is interesting to point out that, when the snow cover affects only the southern slope (SNOWsouth), the near-surface southerly wind is present as in the reference simulation and even slightly reinforced (Figure 7d). This comparison underlines the sensitivity of wind circulation to horizontal snow cover heterogeneities. It is therefore complementary of studies by Chazette *et al.* (2005) and Lehner and Gohm (2010), who have shown that a change of the snow cover distribution with altitude influences the circulations by modifying the surface albedo which may generate a horizontal return flow out of the slope layer. Finally, all these results highlight that high-resolution snow cover fields are necessary to ensure an accurate representation of wind circulations within a valley. The quantification of the impact of snow cover on pollutant transport will be analysed in Part II.

5.2 | Valley scale

The characterization of the flows developed at the valley scale is proposed in two steps with (i) a mass budget to quantify the exchanges between the basin and the surrounding valleys, and (ii) a detailed analysis of

the night-time flow structure in order to investigate the complex layout illustrated from observations in section 3.2.

5.2.1 | Mass budget

A mass budget is computed in order to quantify the exchanges of mass associated with thermally driven circulations at the valley scale. The computation is performed over the volume delimited by the four coloured sections drawn in Figure 11. The sections are positioned in order to quantify the fluxes crossing the downstream part of the valley (DOWN) and the three tributary valleys (MGV, STG and CHX). The volume is vertically bounded at 1500 m a.s.l., this altitude being the average elevation of mountain ranges surrounding the basin as well as the average elevation of the capping inversion during the stagnation stage of IOP1 (not shown). The resulting computation volume represents a total air mass of around 96×10^9 kg.

The continuity equation combined with Ostrogradsky's theorem gives:

$$\int_{\mathcal{V}} \frac{\partial \rho}{\partial t} d\mathcal{V} + \oint_S \rho \mathbf{v} \cdot \mathbf{n} dS = 0, \quad (1)$$

with ρ the air density, \mathbf{v} the wind vector, \mathcal{V} the air volume delimited by the surface S and \mathbf{n} the vector normal to the surface. In the present case, Equation 1 becomes:

$$\int_{\mathcal{V}} \frac{\partial \rho}{\partial t} d\mathcal{V} + M_{\text{DOWN}} + M_{\text{MGV}} + M_{\text{STG}} + M_{\text{CHX}} + M_{\text{TOP}} = 0. \quad (2)$$

The terrain-following coordinate system used in Meso-NH is well adapted for horizontal mass fluxes computation (M_{DOWN} , M_{MGV} , M_{STG} , M_{CHX}), but the direct computation of vertical flux at the volume top (M_{TOP}) is a delicate exercise because model levels do not correspond to a fixed altitude. Since the time evolution of the average density is close to zero (not shown), M_{TOP} is determined as the difference between the flux crossing the downstream

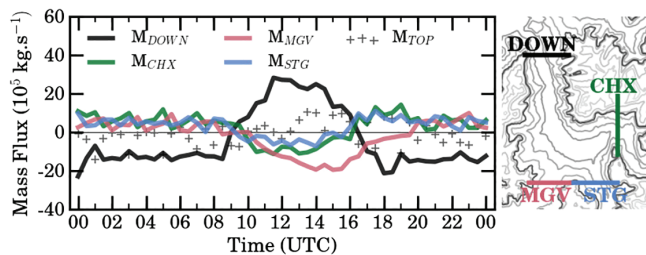


FIGURE 11 Temporal evolution of the horizontal mass fluxes crossing the sections represented on the right-hand panel during the second day of the reference simulation. M_{TOP} represents the vertical mass flux at 1500 m a.s.l. (volume top), indicated by the darker contour on the right-hand panel. Positive (negative) mass fluxes represent an input (output) of air mass for the basin

section and those flowing through the three tributary valleys.

Mass fluxes computed for the REF simulation are drawn in Figure 11 with positive values representing an incoming mass flux with respect to the basin. The analysis is conducted in two parts with the comparison between the different simulations of (i) the air mass vented out of the basin by UVW systems developed in the tributary valleys during the daytime period of ventilation (T_{day}) and (ii) the air mass flowing towards the downstream section by the DVW developed during the night-time period of ventilation (T_{night}). T_{day} is defined as the period of the day during which the basin is filled from its downstream section ($M_{DOWN} > 0$) or drained by its tributary valleys ($M_{MGV,STG,CHX} < 0$). This period has to be determined for each section independently as it depends on the local characteristics of the associated UVW and DVW systems as shown in Figure 11. T_{night} is defined as the remainder of T_{day} from 24 hr. The total air masses flowing through the different valleys during these periods are derived along with the hourly average mass fluxes. These quantities are reported in Table 2 for the daytime period and Table 3 for the night-time period. The results can be summarized in these two tables because mass fluxes in every simulation show similar temporal trends (not shown). The SNOW-south simulation will not be presented in detail as the associated masses and fluxes are between those of the simulations REF and SNOW.

5.2.2 | Daytime exchanges from the basin towards the tributary valleys

In REF, the basin is filled by its downstream section between 0900 and 1600 UTC (Figure 11) leading to a total input of 46.6×10^9 kg of air which represents approximately half of the total basin air mass. In the tributary

valleys, T_{day} appears 3 hr longer for the Megève valley than for the Saint-Gervais and Chamonix valleys. In fact, the total air mass vented out by the Megève valley represents approximately 75% of the mass entering by the downstream section. This value illustrates the large influence of the tributary valley on the main along-valley flux as reported by Zängl (2004). The air mass flowing through the Megève valley is more than 4 and 2 times higher than the air masses flowing through Saint-Gervais and Chamonix respectively. These values highlight a considerable imbalance in the mass distribution between the three tributary valleys which may result from (i) thermal effects with the Megève valley having a more favourable sun exposure while Saint-Gervais and Chamonix both lie within the Mont Blanc shadow, and (ii) inertial effects with a privileged trajectory of the UVW towards the Megève valley because of its relative alignment with the downstream linear section of the basin. This air mass imbalance raises the question of the relative exposure of the three tributary valleys to the pollutant accumulated within the basin at night, which will be further analysed in Part II through a passive tracer tracking. Vertical exchanges at the volume top (M_{TOP}) appear positive on average over the daytime period and negative at night (Figure 11). However, these values remain difficult to interpret as vertical flows may develop in the basin centre to compensate the flux divergence induced by the along-slope circulation (Schmidli and Rotunno, 2010; Serafin and Zardi, 2010; Arduini *et al.*, 2016).

In MARCH, an increase by a factor 2 of the total air mass entering within the basin by the downstream section is observed along with an increase of the hourly-averaged mass flux which becomes higher than 10×10^9 kg·hr⁻¹. This augmentation is in agreement with the UVW intensification reported from observations (cf. Figure 3) and implies that, under the radiative forcing of March, the basin air mass can be entirely renewed during the daytime. Another important change is that the early spring radiative forcing generates a change in the mass distribution between the three tributary valleys. In particular, a more balanced export from the basin towards the Chamonix and Megève valleys is observed with a ratio $MASS_{Mgv}/MASS_{Chx} = 1.2$ instead of 2.2 in the reference simulation. The impact of this evolution on the transport of pollutant towards the Chamonix valley will be further discussed in Part II.

The little change between simulations REF and LESSstable indicates that the initial thermal stability does not represent a critical parameter for the daytime basin ventilation by the UVW systems. A reduction by more than 1 hr of T_{day} is, on the contrary, observed in SNOW along with a diminution of the total mass entering the basin, but

	REF		MARCH		LESSstable		SNOW	
	T_{day}	Mass; Flux	T_{day}	Mass; Flux	T_{day}	Mass; Flux	T_{day}	Mass; Flux
DOWN	7	46.6; 6.7	9.0	96.7; 10.7	6.5	47.9; 7.4	6.5	34.8; 5.4
MGV	9	36.7; 4.1	9.5	51.4; 5.4	9.5	38.3; 4.1	7.5	29.4; 3.9
STG	6	8.6; 1.4	6.5	25.5; 3.9	5.0	8.2; 1.6	4.5	7.1; 1.4
CHMX	6	16.8; 2.8	8.5	41.5; 4.9	6.5	16.5; 2.5	5.0	12.3; 2.5

TABLE 2 Period of daytime ventilation (T_{day} , expressed in hours), total air mass (10^9 kg) flowing through the section during T_{day} , and hourly average air mass fluxes (10^9 kg·hr⁻¹) determined for every section in simulations REF, MARCH, LESSstable and SNOW

	REF		MARCH		LESSstable		SNOW	
	T_{night}	Mass; Flux	T_{night}	Mass; Flux	T_{night}	Mass; Flux	T_{night}	Mass; Flux
DOWN	17.0	80.2; 4.7	15.0	94.0; 6.3	17.5	78.8; 4.5	17.5	69.4; 4.0

TABLE 3 As Table 2, but for horizontal air mass transport towards the downstream basin section occurring during the night-time period of ventilation (T_{night})

with no significant modification of the mass partitioning between the tributary valleys.

5.2.3 | Night-time exchanges from the basin towards the downstream valley

In the reference simulation, 80.2×10^9 kg of air is vented out towards the downstream section of the basin during night-time (Table 3). This mass represents 83% of the total air mass contained in the volume used for mass budget computation (96×10^9 kg). This export of mass is more effective in MARCH with an augmentation by 17% of air mass transferred towards the downstream section. As during daytime, there is no significant change between the total mass exported in REF and LESSstable, suggesting that the initial thermal stability does not play a significant role in horizontal mass exchanges at the valley scale. Under snow cover situations (SNOW), the total mass exported decreases by 13% in comparison with REF, despite a slight increase in the night-time ventilation period. The snow finally reduces air mass exchanges occurring during both daytime and night-time.

Bearing in mind the assessment of the impact of flows on pollutant dispersion, it is necessary to analyse their detailed structure within the basin. This structure is particularly complex at night, as pointed out by observations. The next section will therefore focus on night-time.

5.2.4 | Night-time wind structure

Reference simulation. Scanning Doppler wind lidar observations have revealed a complex night-time wind structure with a down-valley jet flowing above a quiescent air mass and running along the northern sidewall of the basin, while a flow in the opposite direction is observed

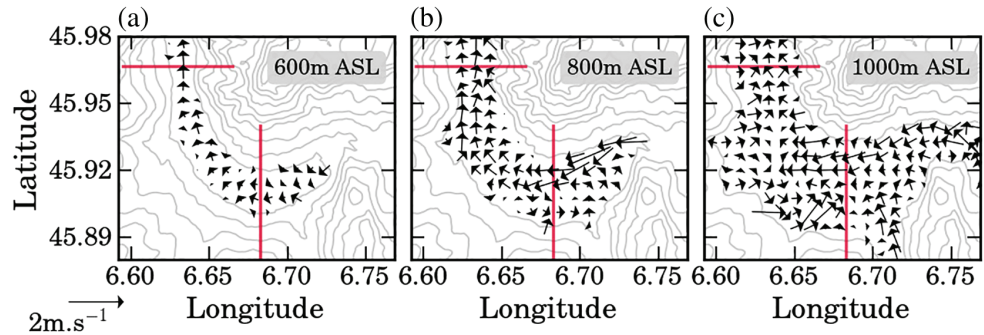
on the southern side (Figure 4). The analysis of the flow organization is proposed from vertical (Figure 6) and horizontal (Figure 12) cross-sections of time-averaged flows over the 2100–0800 UTC period in the reference simulation.

The vertical cross-sections are extracted in the curved basin sector (Figure 6a) and in the more linear western branch (Figure 6b). Figure 6a confirms that the main features of the vertical along-valley flow structure reported from observations in Figure 4 are present in the reference simulation. In addition to the upper DVW running around 800 m a.s.l., this cross-section illustrates the presence of a near-surface DVW developed over the first 50 m a.g.l. which cannot be assessed from observations because of missing data from sonic anemometers at night. In the western branch of the basin, the two superimposed down-valley flows are also present but differ from the basin centre with (i) a more intense near-surface wind with average intensity almost doubled, (ii) a less intense upper jet flowing at a lower elevation, and (iii) a change in the upper jet position centred over the basin width.

The horizontal cross-section at 800 m a.s.l. presented in Figure 12b suggests that the upper jet blowing from the DVW blowing from the Chamonix valley. A comparison of the density of each air mass associated with the DVWs flowing along the tributary valleys was performed in order to determine the equilibrium elevations of these flows within the basin (not shown). It appears that the Chamonix DVW cannot penetrate the lowest atmospheric basin levels because of thermal stratification. This explains, along with its more elevated origin, the upper-jet elevation within the basin. In addition, the upper-jet trajectory is influenced by the convergence of the DVW running along the Saint-Gervais valley which has a similar equilibrium altitude within the basin. This convergence, probably as well as inertia, contributes to the confining of the upper jet near the northern sidewall of the basin.

FIGURE 12

Night-time-averaged (2100–0800 UTC) horizontal cross-sections of the night-time wind structure determined at (a) 600 m, (b) 800 m and (c) 1,000 m a.s.l. for the reference simulation. The red lines indicate the position of the vertical cross-sections displayed in Figure 6



This convergence also leads to the formation of a recirculation cell in the curved sector of the basin explaining the red core observed in Figure 6a. At 800 m a.s.l. in the western branch of the basin, this upper jet does not interact with the DVW from the Megève valley. Its trajectory is therefore undisrupted. Rather, the Megève DVW blows at a higher elevation (1000 m a.s.l.) due to its lower relative density leading to complex flow interactions, as can be seen in Figure 12c. Finally, the complementary analysis of Figures 6 and 12 suggests that the upper jet has a non-local origin and that its trajectory is more constrained in the curved section of the basin due to morphological characteristics of the area, including the presence of tributary valleys.

Conversely, the near-surface DVW is likely to form locally from the katabatic winds' convergence within the basin. Figure 6 shows that this near-surface flow is stronger in the western branch of the basin than in its eastern part. This basin-scale difference may be due to the more linear shape of the western part which is more favourable for the establishment of a drainage flow than the almost enclosed eastern curved part (as shown in Figure 12a), this orographic constraint being known to inhibit the along-valley circulation (Whiteman *et al.*, 2004; De Wekker and Kossmann, 2015). Another possible cause is the time, and therefore the distance, needed for the drainage flow to establish within the basin starting from its closed east side.

Process analysis. The comparison of the night-time wind structure is proposed in Figure 13 in the form of jet contours determined using $-0.5 \text{ m}\cdot\text{s}^{-1}$ as a threshold over the south–north and west–east cross-sections shown in Figure 6 for simulations REF, MARCH, LESSstable and SNOW. The positions of the maximum intensities are indicated by crosses.

In the basin centre (Figure 13a), the upper jet prevails over the near-surface flow in all the tested configurations with jet nose intensities above $1 \text{ m}\cdot\text{s}^{-1}$ whilst the near-surface components barely reach $0.5 \text{ m}\cdot\text{s}^{-1}$. As a result, this vertical flow layout cannot be considered

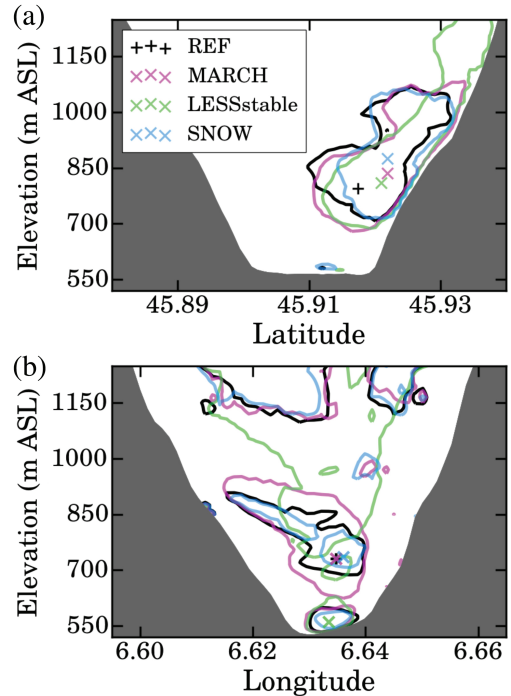


FIGURE 13 Nighttime-averaged (2100–0800 UTC) vertical cross-sections of the DVW contours determined using $-0.5 \text{ m}\cdot\text{s}^{-1}$ as a threshold over (a) a south–north cross-section in the central curved sector and (b) a west–east cross-section in the western branch of the basin for the simulations REF, MARCH, LESSstable and SNOW. The crosses represent the jet maximum positions

as specific to wintertime conditions. However, the upper jet shows a lowering of its base in LESSstable and MARCH simulations. This is consistent with the scanning lidar observations presented in Figure 4b and should increase the ventilation of the lower atmospheric layers. In addition, an intensification of this upper jet occurs in March with maximum and average intensities reaching $1.56 \text{ m}\cdot\text{s}^{-1}$ and $0.85 \text{ m}\cdot\text{s}^{-1}$ respectively instead of 1.06 and $0.67 \text{ m}\cdot\text{s}^{-1}$ in REF.

In the western part of the basin (Figure 13b) the near-surface jet is systematically stronger than in the basin centre, indicating that this feature occurs in every tested

configuration. However the LESSstable simulation differs from the other simulations since the maximum intensity is reached in the near-surface flow and no longer in the upper jet. As a result, the initial stability plays a role in the flow structure developed at a fine scale with the establishment of more intense near-surface flows under a less stratified environment.

Oscillations, stagnation and recirculation indices. An interesting feature which remains to be mentioned is the global oscillating system illustrated in Figure 14a. This figure shows the time evolution of the simulated horizontal wind averaged within the first 100 m a.g.l. represented by vectors (a westerly wind pointing towards the right, a southerly wind towards the top) in the REF simulation. The time series are displayed for the five locations indicated in Figure 1 by black stars. This figure underlines the apparently disorganized wind pattern developed at the basin centre (SITE1) with change in both the wind intensity and direction. Contrarily, in the western part of the basin (SITE4), there are changes in intensity but not in direction with the flow remaining mainly down-valley. These oscillations, mainly present in the centre of the basin, could be another contribution to the weakening of the low-level flow compared to the western branch of the valley (Figure 6). This result, combined with the near-surface flow intensification under less stable conditions mentioned before, reflects a relationship between thermal stability, oscillating system, jet elevation and intensity. An additional dedicated study would be needed to accurately characterize this relationship.

In the tributary valleys, wind oscillations are also present, but the average flows generally have a more intense DVW suggesting a more effective night-time ventilation. A Fast Fourier Transform analysis suggests that the oscillation main period is close to 2.15 hr in the tributary valleys, while it appears to be less defined within the basin as shown in Figure 14b (SITE1 and SITE4). These oscillations were also observed during the field experiment and part of them could be related to a phenomenon such as an atmospheric seiche developed at the basin scale (Whiteman *et al.*, 2008; Lareau and Horel, 2015).

On average through the night, oscillations in the wind direction are associated with air mass stagnation, as shown by the stagnation and recirculation indices presented in Figure 15 for the REF simulation. Those indices are derived across the 2100–0800 UTC period within the first 100 m a.g.l. following the definitions of Allwine and Whiteman (1994):

$$S = T \sum_{j=t_0}^{t_0+n} (u_j^2 + v_j^2)^{\frac{1}{2}}, R = 1 - \frac{(T \sum_{j=t_0}^{t_0+n} u_j + T \sum_{j=t_0}^{t_0+n} v_j)^{\frac{1}{2}}}{S}, \quad (3)$$

with T the temporal resolution (30 min here), n the number of time steps from t_0 (2100 UTC) to $t_0 + n$ (0800 UTC), and u_j and v_j the horizontal wind components. The stagnation index (S) is expressed in km and represents the distance crossed by a particle whilst the recirculation index (R) ranges between 0 (no recirculation) and 1 (complete recirculation).

The stagnation index appears systematically higher than 30 km in the tributary valleys whilst it is reduced by at least 50% (10–15 km) within the basin. The recirculation index is also systematically lower than 0.2 in the tributary valleys, highlighting their high potential for ventilation. On the contrary, large variations of recirculation index are present within the basin with R above 0.8 in the easternmost sector, R in the range 0.4–0.6 in the curved central part, and R lower than 0.2 in the western linear section. This spatial evolution clearly indicates a basin-scale heterogeneity in the degree of ventilation which gradually decreases from the west to the east of the basin. Similar patterns have been observed in every simulation (not shown).

The night-time flow layout developed within the basin therefore results from interactions between drainage flows originating from the tributary valleys which run at different elevations depending on densities relative to the basin atmosphere. In addition, the valley curvature within the basin participates in the formation of shear zones because of the inertial centrifugal force as illustrated in Figure 12c. Basin-scale heterogeneities in the circulation patterns are observed between the curved eastern part of the basin and the western branch. The latter is favourable for more intense surface flows whilst the former is characterized by wind oscillations and stagnation in the lower atmosphere and a recirculation cell above. Finally, local circulations reflect the complex orographic arrangement of the basin.

6 | DISCUSSION AND CONCLUSIONS

The present study aims to understand the flow structure observed within a complex Alpine basin of the Arve River valley investigated during the Passy-2015 field experiment. This basin frequently experiences severe pollution episodes under wintertime quiescent conditions whilst the surrounding tributary valleys appear to be less impacted. This small-scale pollution heterogeneity raises the question of the influence of the complex orography (the basin itself being composed of a linear section followed by a curved sector located at the confluence of tributary valleys) on local dynamics which may in turn favour the ventilation or the stagnation of air masses over restricted areas.

FIGURE 14 (a) Temporal evolution of the horizontal wind vertically averaged over the first 100 m a.g.l. of the five vertical profiles whose locations are represented by black stars in Figure 1 and (b) the associated power spectrum for the REF simulation

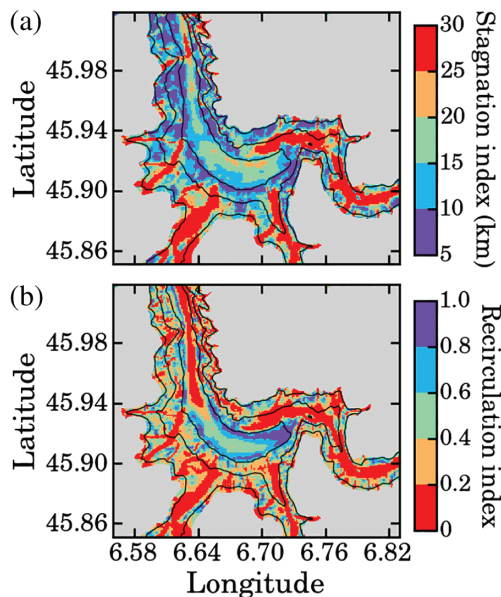
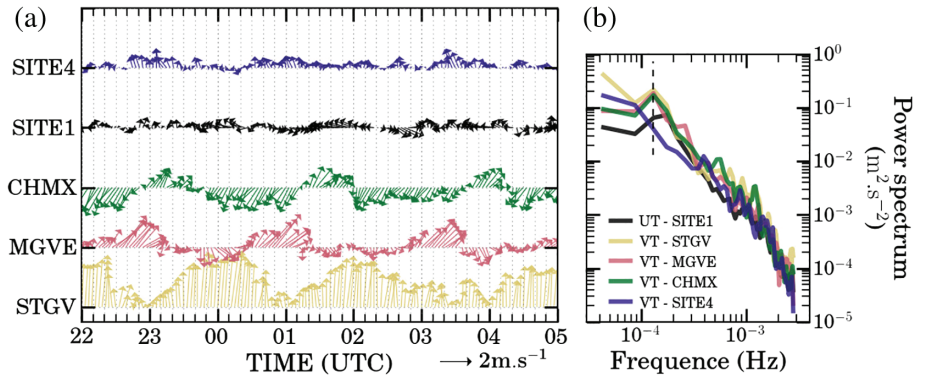


FIGURE 15 (a) Stagnation and (b) recirculation indices determined over the night-time period (2100–0800 UTC) within the first 100 m a.g.l. for the REF simulation

In this framework, a set of semi-idealized high-resolution numerical simulations are run in order to focus on local thermally driven circulations. The reference simulation aims to reproduce favourable conditions for pollution accumulation (persistent temperature inversion, clear-sky conditions, wintertime radiative forcing) based on those encountered during the IOP1 of the campaign. In addition, various experiments are conducted so as to determine to what extent the circulations are modified by weaker initial stratification, early spring radiative forcing, or snow-covered situations. Despite its simplified configuration, this set of simulations allows us to reproduce the main daytime and night-time wind patterns observed during the Passy-2015 field experiment and to clarify their origin. It also raises new questions about their impacts on pollution transport which will be investigated in a companion paper (Part II).

The analysis of the flows developed during the daytime period raises the question of the relative importance of pollutant transport by along-slope and along-valley wind systems. The anabatic winds mainly develop along the south- and east-facing basin sidewalls under the radiative forcing of February. This along-slope circulation drives a near-surface southerly flow developed at the basin bottom which results from the flux divergence generated by the unequally developed anabatic winds. The snow cover appears as an important feature since it may (a) inhibit this near-surface southerly wind layer when the snow is present over the entire domain because of an overall anabatic weakening, or (b) slightly reinforce this component when the snow cover is restricted to the north-facing shaded slopes. This evolution may in turn favour near-surface pollution accumulation or pollutant advection along the sunlit sidewalls. Under early spring radiative forcing, a lengthening of the anabatic regime is observed along with the establishment of up-slope flows over the entire basin sidewalls, even if intensity heterogeneities persist due to spatial variation in sun exposure. This evolution could generate (a) a more effective vertical export of pollutant, or (b) a subsidence motion in the valley core developed to compensate the divergence flux which could favour a re-incorporation of the pollutants within the basin volume. At the valley scale, a mass budget has been computed in order to quantify the exchanges of air mass between the basin and the surrounding tributary valleys. Under the radiative forcing of February, the air mass entering the basin by its downstream section represents approximately half of the total basin air mass. More than half of this mass is deflected to the Megève tributary valley thereby reducing the mass flowing through the eastern part of the basin and the two other tributary valleys. This deflection may result from morphological features as the Megève valley is more aligned with the downstream section and has favourable sun exposure. This imbalance raises the question of the relative exposure of the three tributary valleys to the pollution accumulated within the basin at night. These dynamics evolve under the early

spring radiative forcing with (a) an overall increase of mass flowing through the basin, and (b) a more equilibrated distribution of the mass exported towards the three tributary valleys. This evolution may therefore lead to a more effective transport of pollutant from the basin towards these tributary valleys under early spring conditions.

Over the night-time period, the mass budget has shown that approximately 80% of the basin air mass is vented out towards the downstream section of the valley. However, the refined analysis of the flow structure highlights a complex organization resulting in multiple morphological constraints. In particular, a three-layer wind structure has been observed with (a) a near-surface down-valley flow developed within the first tens of metres above the ground, (b) an intermediate quiescent layer subject to wind direction oscillations, and (c) an upper down-valley jet blowing 200 m above the ground. The upper down-valley jet has a non-local origin and results from the convergence, relative density and inertia of drainage flows running along the tributary valleys. The upper-jet trajectory appears very constrained within the curved sector of the basin due to the orientation of tributary valleys which favour the development of re-circulation cells. The near-surface down-valley flow is likely of local origin and appears more intense in the western linear section while the quiescent layer prevails in the curved part of the basin. The process analysis has shown that this near-surface flow intensifies as the thermal stability decreases. This basin-scale asymmetry is associated with wind oscillations that seem more marked in the curved section of the basin. As a consequence, the air masses in the linear basin section appear as more favourable to ventilation, whereas those in the curved sector are associated with a high degree of recirculation. These basin-scale circulation heterogeneities may have a significant impact on pollutant transport depending on the emission source location.

In summary, this study shows that the local circulations developed within the basin largely depend on the particular complex orography with (a) a daytime two-layer wind structure driven by large variation in sun exposure, and (b) a night-time three-layer wind structure influenced by the tributary valleys and the along-basin morphological variations. The ultimate goal is to address the influence of wind dynamics on pollutant transport. Due to the complexity of the local effects, it would be relevant to classify in terms of importance the main processes driving the dispersion of pollutants. This objective will be the purpose of Part II through a passive tracer tracking which will aim to determine how the tracers are vertically transported within a given area (basin, tributary valleys) and horizontally transferred between these different areas.

ACKNOWLEDGEMENTS

The Passy-2015 field experiment was supported by ADEME through the French national programme LEFE/INSU and by METEO-FRANCE. We thank the cities of Passy and Sallanches for their kind support. The field experiment was led by CNRM while LEGI was the principal investigator of the LEFE/INSU project. Data are managed by SEDOO at Observatoire Midi-Pyrénées (<http://passy.sedoo.fr>; accessed 27 December 2019). We thank all the teams involved in the field experiment: GMEI/LISA, GMEI/4M, GMEI/MN-PCA and GMEI/TRAMM at CNRM; LEGI, IGE, Atmo Auvergne-Rhone-Alpes and NCAS (UK). We are grateful to Stéphanie Faroux and Aaron Boone for their help in surface initialization, as well as the Meso-NH support team.

CONFLICT OF INTEREST

The authors declare no conflict of interest.

ORCID

Tiphaine Sabatier  <https://orcid.org/0000-0001-8489-6331>

REFERENCES

- Alexandrova, O.A., Boyer, D.L., Anderson, J.R. and Fernando, H.J. (2003) The influence of thermally driven circulation on PM10 concentration in the Salt Lake valley. *Atmospheric Environment*, 37, 421–437.
- Allwine, K.J. and Whiteman, C.D. (1994) Single-station integral measures of atmospheric stagnation, recirculation and ventilation. *Atmospheric Environment*, 28, 713–721.
- Arduini, G., Chemel, C. and Staquet, C. (2017) Energetics of deep Alpine valleys in pooling and draining configurations. *Journal of the Atmospheric Sciences*, 74, 2105–2124.
- Arduini, G., Staquet, C. and Chemel, C. (2016) Interactions between the night-time valley-wind system and a developing cold-air pool. *Boundary-Layer Meteorology*, 161, 49–72.
- Atmo-AURA (2015). *Diagnostic annuel – Bilan de la qualité de l'air 2015. Technical Report Atmo-Auvergne Rhones Alpes*. <https://www.atmo-auvergnerhonealpes.fr/publications/diagnostic-annuel-bilan-de-la-qualite-de-lair-2015-region-rhone-alpes>; accessed 27 December 2019.
- Bader, D.C. and Whiteman, C.D. (1989) Numerical simulation of cross-valley plume dispersion during the morning transition period. *Journal of Applied Meteorology*, 28, 652–664.
- Billings, B.J., Grubišić, V. and Borys, R.D. (2006) Maintenance of a mountain valley cold pool: a numerical study. *Monthly Weather Review*, 134, 2266–2278.
- Blein, S. (2016). Experiment and modelling of stable atmospheric boundary layer on complex terrain: the turbulent katabatic wind process. Doctoral thesis, Université Grenoble Alpes, France. Available at: <https://tel.archives-ouvertes.fr/tel-01622676>; accessed 27 December 2019.

- Brun, C., Blein, S. and Chollet, J.-P. (2017) Large-eddy simulation of a katabatic jet along a convexly curved slope. Part 1: Statistical results. *Journal of the Atmospheric Sciences*, 74, 4047–4073.
- Chazette, P., Couvert, P., Randriamiarisoa, H., Sanak, J., Bonsang, B., Moral, P., Berthier, S., Salanave, S. and Toussaint, F. (2005) Three-dimensional survey of pollution during winter in French Alps valleys. *Atmospheric Environment*, 39, 1035–1047.
- Chemel, C., Arduini, G., Staquet, C., Largeron, Y., Legain, D., Tzanos, D. and Paci, A. (2016) Valley heat deficit as a bulk measure of wintertime particulate air pollution in the Arve river valley. *Atmospheric Environment*, 128, 208–215.
- Chow, F.K., Weigel, A.P., Street, R.L., Rotach, M.W. and Xue, M. (2006) High-resolution large-eddy simulations of flow in a steep Alpine valley. Part 1: methodology, verification, and sensitivity experiments. *Journal of Applied Meteorology and Climatology*, 45, 63–86.
- Clements, C.B., Whiteman, C.D. and Horel, J.D. (2003) Cold-air-pool structure and evolution in a mountain basin: Peter Sinks, Utah. *Journal of Applied Meteorology*, 42, 752–768.
- Colella, P. and Woodward, P.R. (1984) The piecewise parabolic method (PPM) for gas-dynamical simulations. *Journal of Computational Physics*, 54, 174–201.
- Colette, A., Chow, F.K. and Street, R.L. (2003) A numerical study of inversion-layer breakup and the effects of topographic shading in idealized valleys. *Journal of Applied Meteorology*, 42, 1255–1272.
- Crosman, E.T. and Horel, J.D. (2010) Sea and lake breezes: A review of numerical studies. *Boundary-Layer Meteorology*, 137, 1–29.
- Cuxart, J. (2015) When can a high-resolution simulation over complex terrain be called LES?. *Frontiers in Earth Science*, 3, 87.
- Cuxart, J., Bougeault, P. and Redelsperger, J.-L. (2000) A turbulence scheme allowing for mesoscale and large-eddy simulations. *Quarterly Journal of the Royal Meteorological Society*, 126, 1–30.
- De Wekker, S.F.J. and Kossmann, M. (2015) Convective boundary-layer heights over mountainous terrain – a review of concepts. *Frontiers in Earth Science*, 3(77). <https://doi.org/10.3389/feart.2015.00077>
- Deardorff, J.W. (1974) Three-dimensional numerical study of turbulence in an entraining mixed layer. *Boundary-Layer Meteorology*, 7, 199–226.
- Defant, F. (1949). A theory of slope winds, along with remarks on the theory of mountain winds and valley winds. English translation in *Alpine Meteorology: translations of classic contributions by A. Wagner, E. Ekhardt and F. Defant (1984)*. Whiteman, C.D., Dreiseitl, E. (eds), Pacific Northwest Laboratory, Richland, WA.
- Duine, G.-J., Hedde, T., Roubin, P., Durand, P., Lothon, M., Lohou, F., Augustin, P. and Fourmentin, M. (2017) Characterization of valley flows within two confluent valleys under stable conditions: observations from the KASCADE field experiment. *Quarterly Journal of the Royal Meteorological Society*, 143, 1886–1902.
- Faroux, S., Kaptué Tchuenté, A.T., Roujean, J.-L., Masson, V., Martin, E. and Le Moigne, P. (2013) ECOCLIMAP-II/Europe: a twofold database of ecosystems and surface parameters at 1 km resolution based on satellite information for use in land surface, meteorological and climate models. *Geoscientific Model Development*, 6, 563–582. <https://doi.org/10.5194/gmd-6-563-2013>
- Fouquart, Y. and Bonnel, B. (1980) Computations of solar heating of the Earth's atmosphere – a new parameterization. *Beiträge zur Physik der Atmosphäre*, 53, 35–62.
- Gal-Chen, T. and Somerville, R.C. (1975) Numerical solution of the Navier–Stokes equations with topography. *Journal of Computational Physics*, 17, 276–310.
- Giovannini, L., Laiti, L., Serafin, S. and Zardi, D. (2017) The thermally driven diurnal wind system of the Adige valley in the Italian Alps. *Quarterly Journal of the Royal Meteorological Society*, 143, 2389–2402. <https://doi.org/10.1002/qj.3092>
- Gohm, A., Harnisch, F., Vergeiner, J., Obleitner, F., Schnitzhofer, R., Hansel, A., Fix, A., Neining, B., Emeis, S. and Schäfer, K. (2009) Air pollution transport in an Alpine valley: Results from airborne and ground-based observations. *Boundary-Layer Meteorology*, 131, 441–463.
- Harnisch, F., Gohm, A., Fix, A., Schnitzhofer, R., Hansel, A. and Neining, B. (2009) Spatial distribution of aerosols in the Inn valley atmosphere during wintertime. *Meteorology and Atmospheric Physics*, 103, 223–235.
- Jiménez, M.A., Cuxart, J. and Martínez-Villagrasa, D. (2019) Influence of a valley exit jet on the nocturnal atmospheric boundary layer at the foothills of the Pyrenees. *Quarterly Journal of the Royal Meteorological Society*, 145, 356–375.
- Lac, C., Chaboureau, J.-P., Masson, V., Pinty, J.-P., Tulet, P., Escobar, J., Leriche, M., Barthe, C., Aouizerats, B., Augros, C., Aumond, P., Franck, A., Bechtold, P., Berthet, S., Soline Bielli, Frédéric Bosseur, Caumont, O., Cohard, J.-M., Colin, J., Couvreur, F., Cuxart, J., Delautier, G., Dauhut, T., Ducrocq, V., Filippi, J.-B., Gazen, D., Geoffroy, O., Gheusi, F., Honnert, R., Lafore, J.-P., Lebeaupin Brossier, C., Libois, Q., Lunet, T., Mari, C., Maric, T., Mascart, P., Mogé, M., Molinié, G., Nuissier, O., Pantillon, F., Peyrillé, P., Pergaud, J., Perraud, E., Pianezze, J., Redelsperger, J.-L., Ricard, D., Richard, E., Riette, S., Rodier, Q., Schoetter, R., Seyfried, L., Stein, J., Suhre, K., Taufour, M., Thouron, O., Turner, S., Verrelle, A., Vié, B., Visentin, F., Vionnet, V. and Wautet, P. (2018) Overview of the Meso-NH model version 5.4 and its applications. *Geoscientific Model Development*, 11, 1929–1969. <https://doi.org/10.5194/gmd-11-1929-2018>
- Lareau, N.P. and Horel, J.D. (2015) Dynamically induced displacements of a persistent cold-air pool. *Boundary-Layer Meteorology*, 154, 291–316.
- Largeron, Y. (2010). Dynamics of the stable Atmospheric Boundary Layer over complex terrain. Application to PM10 pollution episodes in Alpine valleys. Doctoral thesis, Université de Grenoble, France. Available at: <https://tel.archives-ouvertes.fr/tel-00606115>; accessed 27 December 2019.
- Largeron, Y., Paci, A., Rodier, Q., Vionnet, V., Sabatier, T. and Legain, D. (2019) Persistent temperature inversions in the Chamonix–Mont Blanc valley during IOPI of the Passy-2015 field experiment (submitted). *Journal of Applied Meteorology and Climatology*.
- Largeron, Y. and Staquet, C. (2016) Persistent inversion dynamics and wintertime PM10 air pollution in Alpine valleys. *Atmospheric Environment*, 135, 92–108.
- Lehner, M. and Gohm, A. (2010) Idealised simulations of daytime pollution transport in a steep valley and its sensitivity to thermal stratification and surface albedo. *Boundary-Layer Meteorology*, 134, 327–351.
- Lehner, M. and Rotach, M. (2018) Current challenges in understanding and predicting transport and exchange in the atmosphere over mountainous terrain. *Atmosphere*, 9, 276.

- Leo, L., Fernando, H. and Di Sabatino, S. (2015) Near-surface flow in complex terrain with coastal and urban influence. *Environmental Fluid Mechanics*, 15, 349–372.
- Masson, V., Le Moigne, P., Martin, E., Faroux, S., Alias, A., Alkama, R., Belamari, S., Barbu, A., Boone, A., Bouyssel, F., Brousseau, P., Brun, E., Calvet, J.-C., Carrer, D., Decharme, B., Delire, C., Donier, S., Essauouini, K., Gibelin, A. and Voldoire, A. (2013) The SURFEXv7. 2 land and ocean surface platform for coupled or offline simulation of earth surface variables and fluxes. *Geoscientific Model Development*, 6, 929–960.
- Mlawer, E.J., Taubman, S.J., Brown, P.D., Iacono, M.J. and Clough, S.A. (1997) Radiative transfer for inhomogeneous atmospheres: RRTM, a validated correlated-k model for the longwave. *Journal of Geophysical Research: Atmospheres*, 102, 16663–16682.
- Nadeau, D.F., Pardyjak, E.R., Higgins, C.W., Huwald, H. and Parlange, M.B. (2013) Flow during the evening transition over steep Alpine slopes. *Quarterly Journal of the Royal Meteorological Society*, 139, 607–624.
- O'Steen, L.B. (2000) Numerical simulation of nocturnal drainage flows in idealized valley–tributary systems. *Journal of Applied Meteorology*, 39, 1845–1860.
- Paci, A., Staquet, C., Allard, J., Barral, H., Canut, G., Cohard, J.-M., Jaffrezo, J.-L., Martinet, P., Sabatier, T., Troude, F., Arduini, G., Burnet, F., Brun, C., Chemel, C., Dabas, A., Donier, J.-M., Garrouste, O., Guillot, R., Largeron, Y., Legain, D., Maurel, W., Tzanos, D., Barrau, S., Barret, M., Barrie, J., Belleudy, A., Bouhours, G., Bourriane, T., Chevrier, F., Douffet, T., Etcheberry, J.-M., Gustave, L., Mazoyer, M., Mercier, S., Moulin, E., Pellan, Y., Piguat, B., Rodier, Q. and Zin, I. (2016) The Passy-2015 field experiment: atmospheric dynamics and air quality in the Arve River valley. *Pollution Atmosphérique*, 231–232. <https://doi.org/10.4267/pollution-atmospherique.5903>
- Pardyjak, E.R., Fernando, H.J.S., Hunt, J.C.R., Grachev, A.A. and Anderson, J. (2009) A case study of the development of nocturnal slope flows in a wide open valley and associated air quality implications. *Meteorologische Zeitschrift*, 18, 85–100. <https://doi.org/10.1127/0941-2948/2009/362>
- Pernigotti, D., Rossa, A.M., Ferrario, M.E., Sansone, M. and Benassi, A. (2007) Influence of ABL stability on the diurnal cycle of PM10 concentration: illustration of the potential of the new Veneto network of MW-radiometers and SODAR. *Meteorologische Zeitschrift*, 16, 505–511. <https://doi.org/10.1127/0941-2948/2007/0204>
- Perrino, C., Catrambone, M., Dalla Torre, S., Rantica, E., Sargolini, T. and Canepari, S. (2014) Seasonal variations in the chemical composition of particulate matter: a case study in the Po valley. Part 1: macro-components and mass closure. *Environmental Science and Pollution Research*, 21, 3999–4009.
- Pinty, J.-P. and Jabouille, P. (1998). A mixed-phased cloud parameterization for use in a mesoscale non-hydrostatic model: simulations of a squall line and of orographic precipitation. In preprints for Conference on Cloud Physics: 14th Conference on Planned and Inadvertent Weather Modification, Everett, WA, pp. 217–220. American Meteorological Society, Boston, MA.
- Porch, W.M., Fritz, R.B., Coulter, R.L. and Gudiksen, P.H. (1989) Tributary, valley and sidewall air flow interactions in a deep valley. *Journal of Applied Meteorology*, 28, 578–589.
- Rampanelli, G., Zardi, D. and Rotunno, R. (2004) Mechanisms of up-valley winds. *Journal of the Atmospheric Sciences*, 61, 3097–3111.
- Rendón, A.M., Salazar, J.F., Palacio, C.A., Wirth, V. and Brötz, B. (2014) Effects of urbanization on the temperature inversion breakup in a mountain valley with implications for air quality. *Journal of Applied Meteorology and Climatology*, 53, 840–858.
- Retallack, C., Calhoun, R., Fernando, H., Rayner, K., Stuart, A., Sutton, J. and Hibberd, M.F. (2010) Flow and pollution transport during Wagerup 2006: a case study. *Meteorological Applications*, 17, 269–278.
- Rucker, M., Banta, R.M. and Steyn, D.G. (2008) Along-valley structure of daytime thermally driven flows in the Wipp valley. *Journal of Applied Meteorology and Climatology*, 47, 733–751.
- Sabatier, T., Largeron, Y., Paci, A., Lac, C., Rodier, Q., Canut, G. and Masson, V. (2020) Semi-idealized simulations of wintertime flow and pollutant transport in an Alpine valley: Passive tracer tracking (Part II). *Quarterly Journal of the Royal Meteorological Society*.
- Sabatier, T., Paci, A., Canut, G., Largeron, Y., Dabas, A., Donier, J.-M. and Douffet, T. (2018) Wintertime local wind dynamics from scanning Doppler lidar and air quality in the Arve river valley. *Atmosphere*, 9, 118.
- Schmidli, J. and Rotunno, R. (2010) Mechanisms of along-valley winds and heat exchange over mountainous terrain. *Journal of the Atmospheric Sciences*, 67, 3033–3047.
- Serafin, S., Adler, B., Cuxart, J., De Wekker, S., Gohm, A., Griso-gono, B., Kalthoff, N., Kirshbaum, D., Rotach, M., Schmidli, J., Stiperski, I., Vecenaj and Zardi, D. (2018) Exchange processes in the atmospheric boundary layer over mountainous terrain. *Atmosphere*, 9, 102.
- Serafin, S. and Zardi, D. (2010) Daytime heat transfer processes related to slope flows and turbulent convection in an idealized mountain valley. *Journal of the Atmospheric Sciences*, 67, 3739–3756.
- Silcox, G.D., Kelly, K.E., Crosman, E.T., Whiteman, C.D. and Allen, B.L. (2012) Wintertime PM2.5 concentrations during persistent, multi-day cold-air pools in a mountain valley. *Atmospheric Environment*, 46, 17–24.
- Stein, J. (2004) Exploration of some convective regimes over the Alpine orography. *Quarterly Journal of the Royal Meteorological Society*, 130, 481–502.
- Steyn, D.G., De Wekker, S.F., Kossmann, M. and Martilli, A. (2013). Boundary layers and air quality in mountainous terrain, Pp. 261–289 in Mountain Weather Research and Forecasting. Chow F., De Wekker S., Snyder B. (eds). Springer, Dordrecht, Netherlands.
- Vionnet, V., Martin, E., Masson, V., Guyomarc'h, G., Naaim-Bouvet, F., Prokop, A., Durand, Y. and Lac, C. (2014) Simulation of wind-induced snow transport and sublimation in Alpine terrain using a fully coupled snowpack/atmosphere model. *The Cryosphere*, 8, 395–415. <https://doi.org/10.5194/tc-8-395-2014>
- Vionnet, V., Martin, E., Masson, V., Lac, C., Bouvet, F.N. and Guyomarc'h, G. (2017) High-resolution large-eddy simulation of snow accumulation in Alpine terrain. *Journal of Geophysical Research: Atmospheres*, 122, 11005–11021. <https://doi.org/10.1002/2017JD026947>
- Wagner, A. (1938) Theory and observation of periodic mountain winds. *Gerlands Beiträge zur Geophysik (Leipzig)*, 52, 408–449.

- English translation in *Alpine Meteorology: translations of classic contributions* by A. Wagner, E. Ekhart and F. Defant (1984). Whiteman, C.D., Dreiseitl, E. (eds). Pacific Northwest Laboratory, Richland, WA.
- Wagner, J., Gohm, A. and Rotach, M. (2015a) The impact of valley geometry on daytime thermally driven flows and vertical transport processes. *Quarterly Journal of the Royal Meteorological Society*, 141, 1780–1794.
- Wagner, J., Gohm, A. and Rotach, M. (2015b) Influence of along-valley terrain heterogeneity on exchange processes over idealized valleys. *Atmospheric Chemistry and Physics*, 15, 6589–6603.
- Weigel, A.P. and Rotach, M.W. (2004) Flow structure and turbulence characteristics of the daytime atmosphere in a steep and narrow Alpine valley. *Quarterly Journal of the Royal Meteorological Society*, 130, 2605–2627.
- Weigel, A.P., Chow, F.K., Rotach, M.W., Street, R.L. and Xue, M. (2006) High-resolution large-eddy simulations of flow in a steep Alpine valley. Part II: Flow structure and heat budgets. *Journal of Applied Meteorology and Climatology*, 45, 87–107.
- Whiteman, C.D. (2000) *Mountain Meteorology: Fundamentals and Applications*. Oxford University Press, Oxford, UK.
- Whiteman, C.D. and Doran, J.C. (1993) The relationship between overlying synoptic-scale flows and winds within a valley. *Journal of Applied Meteorology*, 32, 1669–1682.
- Whiteman, C.D. and Zhong, S. (2008) Downslope flows on a low-angle slope and their interactions with valley inversions. Part 1: observations. *Journal of Applied Meteorology and Climatology*, 47, 2023–2038.
- Whiteman, C.D., Bian, X. and Zhong, S. (1999) Wintertime evolution of the temperature inversion in the Colorado plateau basin. *Journal of Applied Meteorology*, 38, 1103–1117.
- Whiteman, C.D., Pospichal, B., Eisenbach, S., Weihs, P., Clements, C.B., Steinacker, R., Mursch-Radlgruber, E. and Dorninger, M. (2004) Inversion breakup in small rocky mountain and Alpine basins. *Journal of Applied Meteorology*, 43, 1069–1082.
- Whiteman, C.D., Muschinski, A., Zhong, S., Fritts, D., Hoch, S.W., Hahnenberger, M., Yao, W., Hohreiter, V., Behn, M., Cheon, Y., Clements, C.B., Horst, T.W., Brown, W.O.J. and Oncley, S.P. (2008) Metcrax 2006: Meteorological experiments in Arizona's meteor crater. *Bulletin of the American Meteorological Society*, 89, 1665–1680.
- Zängl, G. (2004) A re-examination of the valley wind system in the Alpine Inn valley with numerical simulations. *Meteorology and Atmospheric Physics*, 87, 241–256.
- Zardi, D. and Whiteman, C.D. (2013). Diurnal mountain wind systems, in *Mountain Weather Research and Forecasting*, Chow F., De Wekker S., Snyder B. (eds). Springer, Dordrecht, Netherlands.
- Zhong, S. and Whiteman, C.D. (2008) Downslope flows on a low-angle slope and their interactions with valley inversions. Part 2: numerical modeling. *Journal of Applied Meteorology and Climatology*, 47, 2039–2057.

How to cite this article: Sabatier T, Paci A, Lac C, Canut G, Largeron Y, Masson V. Semi-idealized simulations of wintertime flows and pollutant transport in an Alpine valley: Origins of local circulations (Part I). *QJR Meteorol Soc.* 2020;146:807–826. <https://doi.org/10.1002/qj.3727>